Correcting organ motion artifacts in x-ray CT medical imaging systems by adaptive processing. I. Theory

A. C. Dhanantwari[a)]
Biomedical Sciences Section, Defence and Civil Institute of Environmental Medicine, 1133 Sheppard Avenue West, Toronto, Ontario M3M 3B9, Canada

S. Stergiopoulos[b)]
Biomedical Sciences Section, Defence and Civil Institute of Environmental Medicine, 1133 Sheppard Avenue West, Toronto, Ontario M3M 3B9, Canada and Department of Electrical and Computer Engineering, The University of Western Ontario, London, Ontario N6A 5B9, Canada

I. Iakovidis[c)]
European Commission, DG-IST, Avenue de Beaulieu 29, B-1160 Brussels, Belgium

(Received 31 January 2001; accepted for publication 7 June 2001)

X-ray CT scanners provide images of transverse cross sections of the human body from a large number of projections. During the data acquisition process, which usually takes about 1 s, motion effects such as respiration, cardiac motion, and patient restlessness produce artifacts that appear as blurring, doubling, and distortion in the reconstructed images, and may lead to inaccurate diagnosis. To address this problem several processing techniques have been proposed that require *a priori* knowledge of the motion characteristics. This paper proposes a method, which makes no assumptions about the properties of the motion, to eliminate the motion artifacts. The approach in this paper uses a spatial overlap correlator scheme to accurately track organ motion in computed tomography imaging systems. Then, it is shown that as optimum processing scheme to remove organ motion effects is to apply adaptive interference cancellation (AIC) methods, which treat the output of the spatial overlap correlator as noise interference at the input of the AIC process. Furthermore, an AIC method does not require any kind of periodicity of the motion effects. Synthetic data tests demonstrate the validity of this approach and show that hardware modifications are essential for its implementation in x-ray CT medical imaging systems. [DOI: 10.1118/1.1388892]

Key words: CT scanners, organ motion artifacts, spatial overlap correlator, adaptive interference canceller

I. INTRODUCTION

X-ray computed tomography (CT) is an imaging modality that provides cross-sectional images or ''slices'' of the human body. The patient is placed in between an x-ray source and an array of sensors, the latter measuring the amount of radiation that passes through the body. During the data acquisition process, the source and detectors move around the patient acquiring a large number of x-ray projections, or views. This process assumes stationarity, which is violated when there is organ motion (e.g. cardiac motion, blood flow, respiratory motion, and patient restlessness) during the relatively long (e.g., 0.5–1.5 s) data acquisition time. Thus, the image reconstruction process is adversely affected by the so-called motion artifacts, which appear as blurring, doubling, streaking, and distortion in the reconstructed images; and may lead to inaccurate diagnosis.[1,2]

The intuitive solution to this problem is to speed up the data acquisition process, so that the motion effects become negligible. This requirement, however, cannot be met with current technology; the scan times that are required are simply not realizable even by the most advanced conventional CT scanner today. The only CT scanner that delivers the required speed is the electron beam CT (EBCT), which is not widely available.

Several mathematical techniques have been proposed as solutions to this problem. These techniques usually assume a linear model for the motion, such as translational, rotational, or linear expansion.[3] Some techniques model the motion as a periodic sequence and take projections at a particular point in the motion cycle to achieve the effect of scanning a stationary object (similar to ECG triggering).[4] However, in practical applications motion is much more complex, and these techniques are useful in a very limited number of cases. A more general technique attempts to iteratively suppress the motion effects from the projection data.[5] This method attempts to reduce the assumed spectral characteristics of the motion artifacts. It, however, depends on knowing some properties of the motion *a priori*, and requires a number of iterations to converge. The spectral properties of some complex forms of motion may not necessarily correspond to the model used in this algorithm. Moreover, without proper initialization, the convergence period could be long.

Motion artifacts in magnetic resonance imaging (MRI) for chest scans have been reduced by first defining the motion with a parametric model and then adapting the reconstruction

algorithm to correct for the modeled motion.[6] Ritchie *et al.*[7] attempted to address the problems of CT cardiac and respiratory motion artifacts by using a pixel-specific backprojection algorithm that was conceptually influenced by the MRI motion modeling approach.[6] In the CT case, the frame of reference for the motion was generated by constructing maps that describe the motion of each pixel in the image at the time each projection was measured.[6] These maps then form the basis of a backprojection algorithm that reconstructs each pixel in a frame of reference according to the motion information provided by the maps. However, the method requires substantial manual effort to describe the motion of each pixel and therefore is not practical for x-ray CT medical imaging applications.

The problem of motion artifacts, however, is well known in other types of imaging systems such as RADAR satellites and SONARs.[8,9] In this case, it has been found that the application of synthetic aperture processing increases the resolution of a phased array imaging system and corrects for the motion artifacts as well. Reported results[8,9] have shown that the problem of correcting motion artifacts in synthetic aperture SONAR applications is centered on the estimation of a phase correction factor. This factor is used to compensate for the phase differences between sequential sensor array measurements to coherently synthesize the multiple spatially overlapping measurements into a synthetic aperture.

The approach of this investigation is built around the concept of the spatial overlap correlator (SOC) for x-ray CT data acquisition, which is conceptually based on the spatial overlap correlator in SONARs and RADARs. The SOC may be described as an alternative data acquisition scheme that samples only the motion that is present during the standard x-ray CT data acquisition period. The SOC is implemented in x-ray CT scanners as a two sources concept that provides an accurate estimate of the information associated with any kind of complex organ motion. Since the SOC is a sampling process, the upper limit of the frequency of the sampled organ motion is dependent on the sampling interval of the SOC process, in order to satisfy the Nyquist sampling rate. This process generates a new set of sinograms (or sensor time series) that include only information about motion effects present during the CT data acquisition process. Information about stationary components of the tomographic area of interest is not present in the sinograms (sensor time series) provided by the SOC process. This means that two sets of information (sinograms) are available for further processing. This first is the data sequence from the standard x-ray CT data acquisition and the second the data sequence from the SOC, which contains only the motion that was present during the x-ray CT data acquisition period.

The adaptive interference cancellation (AIC) process[10–13] is commonly used in applications where there is a noisy signal, and it is possible to simultaneously measure both the noisy signal and the noise component individually.[10] Considering the data available from the data acquisition scheme, and the result that is desired, the AIC process appears to be the optimum signal processing scheme to remove the motion measured by the SOC sampling process during the x-ray CT data acquisition period. The data sequence from each detector is treated as a time series. Since there are two data acquisition schemes that are operating concurrently (i.e., the SOC and the standard x-ray CT data acquisition processes), there are two time series available for each detector. The sequence from the standard x-ray CT acquisition is treated as the noisy signal, and the sequence from the SOC process is treated as the interference (noise) in the AIC processing scheme. Furthermore, because the AIC process does not require any kind of periodicity for the motion effects, the processing scheme of this investigation eliminates the requirement for ECG gating that is currently being used by x-ray CT scanners for cardiac imaging applications.

However, the AIC method requires that the data sets be acquired over a number of revolutions of the x-ray CT scanner, as opposed to just one revolution in straightforward x-ray CT image reconstruction. This number is a function of the convergence rate of the adaptive algorithm and is required to be at least two revolutions. Also, implementation of the AIC method in CT scanners requires hardware modifications to allow for the implementation of the two sources concept associated with the SOC. This is discussed analytically in Sec. III.

Moreover, Sec. II provides a theoretical analysis and a physical interpretation of the SOC system concept. The results of an experimental study to exploit this theoretical approach in practical x-ray CT medical imaging applications are discussed in an accompanying paper.[14]

II. THEORETICAL REMARKS

A. Definition of parameters

The data acquisition process in CT applications is depicted in Fig. 1. The projection measurements, $g_n(\sigma_n,\beta_i)$, $(n=1,...,N)$, $(i=1,...,M)$, shown schematically in Fig. 1, are defined as the line integrals along lines passing through the object $f(x,y)$. For a given detector n, projection i, and projection angle β_i, $g_n(\sigma_n,\beta_i)$ is given by Eq. (1). In Eq. (1), $\delta(\cdot)$ represents the Dirac delta function, β_i represents the projection angle, and σ_n represent the angle that detector n makes with the center of the detector arc. The line traced by the ray from the source to the detector is given in Eq. (2), and the integration along this path is reflected in Eq. (1),

$$g_n(\sigma_n,\beta_i)=\int\int f(x,y)\,\delta[x\cos(\beta_i+\sigma_n)+y\sin(\beta_i+\sigma_n)-R\sin(\sigma_n)]\,dx\,dy, \tag{1}$$

$$x\cos(\beta_i+\sigma_n)+y\sin(\beta_i+\sigma_n)=R\sin(\sigma_n). \tag{2}$$

The function $f(x,y)$ is also the function we wish to approximate through the image reconstruction process. The angular step increment between two successive projections of the x-ray scanner is defined by: $\Delta\beta=2\pi/M$, and Δt is the time elapsed between these successive projections, where M is the number of projections taken during the period $T=M\Delta t$ that is required for one full rotation of the source and receiving array around the object $f(x,y)$ that is being imaged.

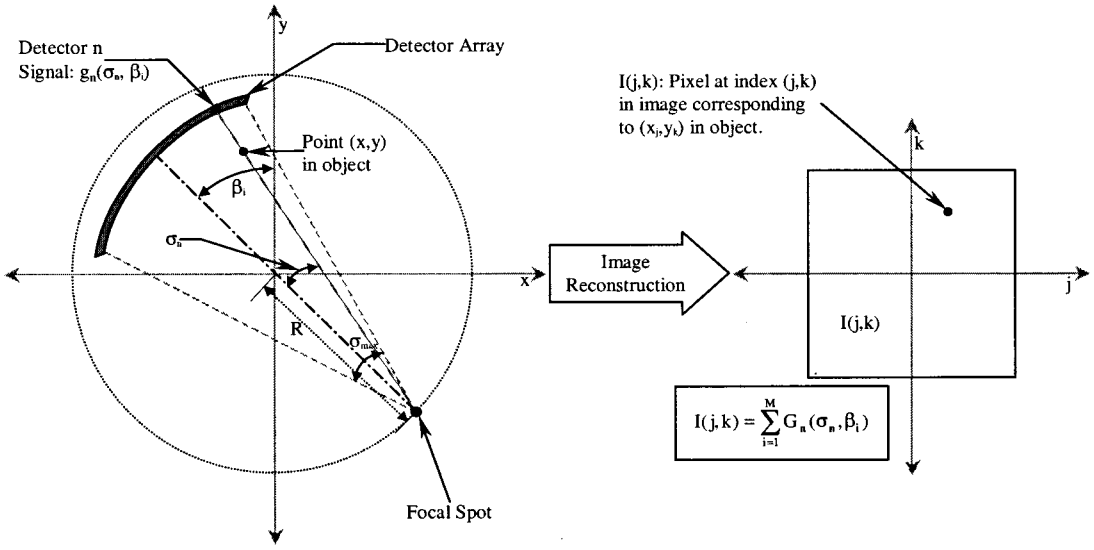

FIG. 1. Schematic diagram of projection function for CT x-ray imaging systems.

In the image reconstruction process the pixel $I(j,k)$ in the actual image, shown at the right hand side of Fig. 1, corresponds to the Cartesian point (x_j, y_k) in the CT scan plane. Given a filter with frequency response $F(n)$, $(n=1,...,N)$, the filtered projection data is given by

$$G_n(\sigma_n, \beta_i) = Ifft[fft(g_n(\sigma_n, \beta_i) \cdot F(n))]. \tag{3}$$

The filtering function used in this investigation is the Ram–Lak filter,[18] cascaded with the Parzen window. The pixel value $I(j,k)$ is given by

$$I(j,k) = \sum_{i=1}^{M} G_n(\sigma_n, \beta_i), \tag{4}$$

where the appropriate modifications have been made to $G_n(\sigma_n, \beta_i)$ to account for geometric effects. For each β_i in Eq. (4), a detector, n, is selected. The angle σ_n, which defines the detector, n, that samples the projection through a point (x_j, y_k), for a given projection angle β_i, is provided by Eq. (5), where (r_d, φ) is the polar representation of (x_j, y_k),

$$\sigma_n = \tan^{-1}\left[\frac{r_d \sin(\beta_i - \varphi)}{R + r_d \cos(\beta_i - \varphi)}\right], \quad \frac{-\pi}{2} \leqslant (\beta_i - \varphi) < \frac{\pi}{2},$$

$$\sigma_n = \tan^{-1}\left[\frac{r_d \sin(\varphi - \beta_i)}{R + r_d \cos(\varphi - \beta_i)}\right], \quad \frac{\pi}{2} \leqslant (\beta_i - \varphi) < \frac{3\pi}{2}. \tag{5}$$

B. Spatial overlap correlator

In SONAR applications,[8,9] it has been shown that the spatial overlap correlator increases the angular resolution (array gain) and reduces artifacts that are caused by scattering and the target's or receiving-array's motion effects. The approach of generating a synthetic aperture is based on computing an appropriate phase correction factor to coherently synthesize overlapping spatial measurements[8] into an equivalent longer physical aperture. Extending this scheme to the case of CT applications is not straightforward. The computation of the factor is still based on the comparison of spatially overlapping measurements at two consecutive time moments during the CT sampling process. This factor tracks the phase or amplitude fluctuations caused by the subject's organ-motion effects, and includes information due to the movement of organs such as the heart and lungs.

Shown in Fig. 2 is the concept of the SOC process for CT applications. This is a data acquisition scheme to obtain an estimate of the motion information for subsequent removal. As shown in Fig. 2, the scheme assumes two physical sources and an array receiver. The two sources follow the same rotational path, although, in Fig. 2, they are depicted as following paths of slightly different radii for the purpose of illustration. The system of two sources-array receiver performs the data acquisition process in a conventional manner. Specifically, at time t_0, which is the starting time of the CT data acquisition process, the array receiver and the two sources are at spatial locations s_1 and s_2, respectively, as shown by the closed dots in Fig. 2. At time $(t_0 + \Delta t)$, where $\Delta t = T/M$ is the elapsed time between two successive firings of the x ray, the two sources will be at locations s_2 and s_3, shown by the lighter dots in Fig. 2. The process is repeated M times throughout the data acquisition period T for one full rotation.

Based on the schematic representation of Fig. 2, the CT measurements corresponding to the spatial location s_2 are obtained twice at times t_0 and $(t_0 + \Delta t)$. This is analogous to taking two consecutive photographs at times t_0 and $(t_0 + \Delta t)$ of a field of view that includes a moving train and other stationary objects, such as trees and houses. If the images from these two photographs are subtracted at the pixel level, then the resulting image will include information about the moving train only. Based on this simplistic interpretation of the information provided by the two source CT measurement system, as depicted in Fig. 2, a comparison (or correlation) of the two spatially overlapping measurements will

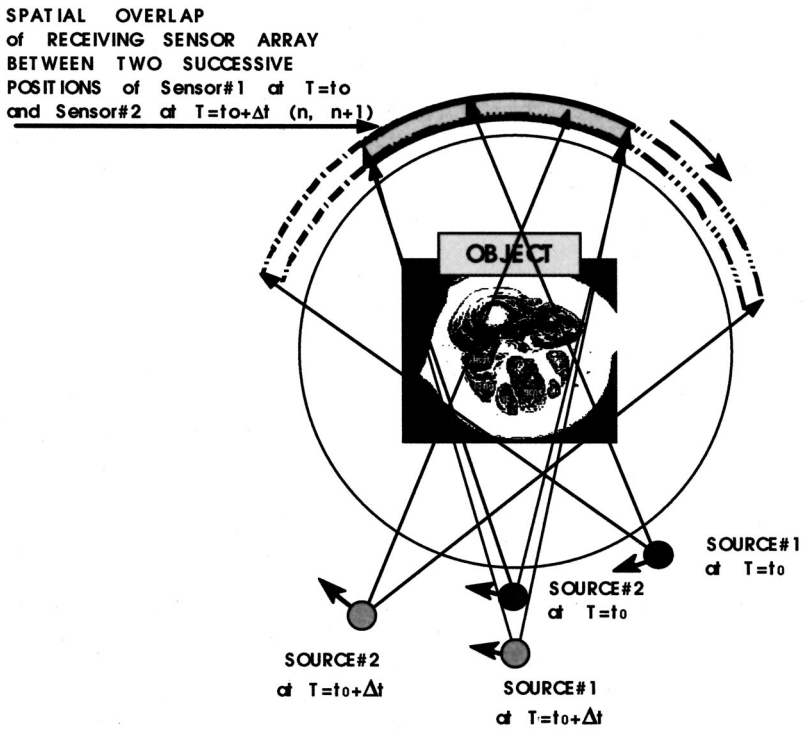

FIG. 2. Two-source concept of spatial overlap correlator for CT x-ray imaging systems.

provide a new set of measurements that should describe any type of organ motion that may have occurred during the time increment Δt. Thus, $1/\Delta t$ is the sampling frequency of the SOC process and indicates that the upper limit of the sampled organ motion frequency is dependent on the time interval Δt in order to satisfy the Nyquist sampling rate.

A time dependency is now included in all the parameters of Eq. (1) to account for the fact that the measured projections may be time varying in the presence of motion. More specifically,

$$\{g_{n_{s2}}(\sigma_n,\beta(t_0+\Delta t),t_o),(n_{s2}=q,q+1,...,N),\}$$
$$\{g_{n_{s1}}(\sigma_n,\beta(t_0+\Delta t),t_o+\Delta t),$$
$$(n_{s1}=1,2,...,N-q),\} \tag{6}$$

are the $(N-q)$ spatially overlapping measurements for the projection angle $\beta(t)$ received by the N-element array at the two successive moments t_o and $(t_o+\Delta t)$, as depicted in Fig. 2. Since s_2 is ahead of s_1 during the data acquisition process, $g_{n_{s1}}(\sigma_n,\beta(t_0+\Delta t),t_o+\Delta t)$ and $g_{n_{s2}}(\sigma_n,\beta(t_0+\Delta t),t_o)$ are spatially overlapping measurements corresponding to the projection angle $\beta(t_o+\Delta t)$. Based on Eq. (1), the time-dependent projection measurements for a fan-beam scanner is expressed by

$$g_n(\sigma(n),\beta(t),t)=\int\int f(x,y,t)\,\delta\{x\cos[\sigma(n)+\beta(t)] + y\sin[\sigma(n)+\beta(t)] - R\sin\sigma(n)\}dx\,dy. \tag{7}$$

In Eq. (7) $\beta(t)$ defines the projection angle, $\sigma(n)$ defines the angle described by the detector in the detector arc, as shown in Fig. 1, $\delta(\cdot)$ is the Dirac delta function, and $f(x,y,t)$, is a time varying tomography object. For fan-beam CT applications, the amplitude difference between the two sets of measurements of Eqs. (6) and (7) is defined by

$$\Delta g_{n_o}(\sigma(n_o),\beta(t),t_o+\Delta t) = g_{n_{s1}}(\sigma(n_{s1}),\beta(t_o+\Delta t),t_o+\Delta t) - g_{n_{s2}}(\sigma(n_{s2}),\beta(t_o+\Delta t),t_o) \quad \text{for } (n_o=1,2,...N-q), \tag{8}$$

where $(n_{s1}=1,2,...,N-q)$ and $(n_{s2}=q,q+1,...,N)$. Note that spatially overlapping measurements are taken at the projection angle $\beta(t_0+\Delta t)$ at times t_0 and $t_0+\Delta t$ to accommodate the SOC scheme. As a result of Eq. (7), and recalling the spatial overlap concept of Eq. (8), which assumes that $\{\beta(t_0+\Delta t)=\beta_{s1}(t_o+\Delta t)=\beta_{s2}(t_o)\}$, $\{\sigma(n)=\sigma(n_{s1})=\sigma(n_{s2})\}$, Eq. (8) takes the form:

$$\Delta g_n(\sigma(n),\beta(t),t_o+\Delta t) = \int\int [f(x,y,t_o)-f(x,y,t_o+\Delta t)]\{\delta\{x\cos[\sigma(n) + \beta(t_o+\Delta t)]+y\sin(\sigma(n) + \beta(t_o+\Delta t)\}-R\sin\sigma(n)\}dx\,dy, \tag{9}$$

where $[f(x,y,t_o)-f(x,y,t_o+\Delta t)]$ indicates the tomographic differences of the time varying object between the time moments t_0 and $(t_0+\Delta t)$.

From this arrangement, for a stationary object, it is evident that this two source configuration will provide spatially identical sets of measurements at all spatial locations, despite being taken at two successive moments in time, separated by

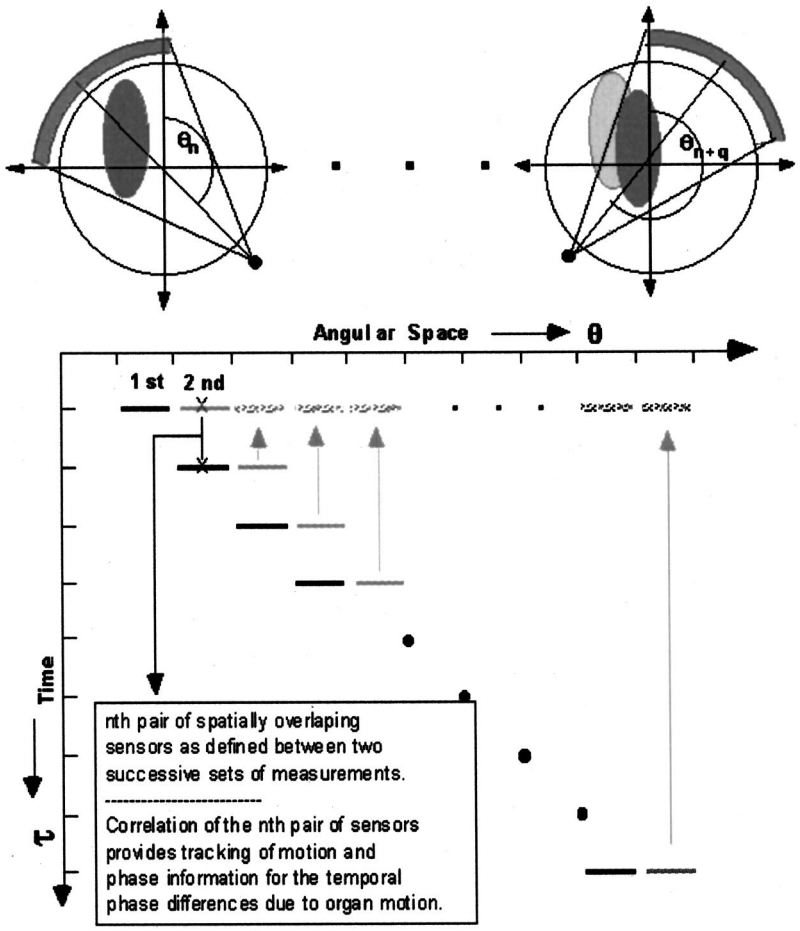

FIG. 3. Graphical representation of the space–time sampling process of the spatial overlap correlator for CT x-ray imaging systems.

Δt. If the measurements of the SOC process depicted in Fig. 2 and defined by Eqs. (8) and (9) are provided at the input of an image reconstruction algorithm, then the resultant image will show the time-dependent changes $[f(x,y,t)-f(x,y,t+\Delta t)]$ (for $t=t_o,\ldots,t_o+T$) that took place during the time period T of the CT data acquisition process. This suggests that image reconstruction of the SOC measurements of Eq. (9) will track only the moving components of the object. The stationary components will have zero contribution and they will not appear in the reconstructed image.

Figure 3 presents a graphical representation of the above-mentioned two dimensional space–time sampling process defined by Eqs. (8) and (9) and Fig. 2. The vertical axis shows the time moments, τ, associated with the angular positions, θ, of the source-array receiver that are shown by the horizontal axis. The black and dark gray sets of line segments along the diagonal of this $\tau-\theta$ plot represent the measurements of a CT scanner at different angular positions. In other words, this is a representation of data acquisition with the two source concept described. Image reconstruction algorithms, however, assume stationarity in the object, or alternatively that these sets of measurements are along a horizontal line of Fig. 3, as shown by the light gray bars (i.e., that they have been acquired instantaneously). However, as shown in Fig. 3, during the data acquisition period of T seconds for one full rotation of the scanner, the object of interest may suffer deformation as is the case of organ motions (i.e., heart, lungs, etc.). Also in Fig. 3 the spatially overlapping measurements of Eqs. (8) and (9) are depicted by the pair of lines that overlap in angular space but are taken at two successive time moments. This process is equivalent to a synthetic aperture processing scheme for SONAR applications.[8,9]

The SOC processing scheme provides both tracking of the phases of the organ motion[14,15] and incremental measurement of any organ motion,[16] which is discussed next. It is also shown that an alternative motion correction method that corrects for organ motion based solely on the tracking of the phase of the motion is a viable alternative.[16]

An obvious organ motion correction scheme is to remove the temporal amplitude and phase differences, due to organ motion effects, between the spatially overlapping sets of measurements. Ideally, this correction process will correct all of the measurements with respect to the first measurement, which is equivalent in moving the diagonal measurements into the same instant in time and along the horizontal line, as shown in Fig. 3, that corresponds to the time moment t_o. This approach has been tested with synthetic data and it has been shown that it is not effective because the number of projections, M, in CT scanners is very large $O(10^3)$. As a result, the propagation of processing and angular errors from

the correction process build up significantly and destroy useful information.

C. Physical interpretation of the measurements provided by the SOC and the conventional CT

At this point it is important to emphasize the relationship between the measurements provided by the SOC that tracks the motion effects and the conventional CT data acquisition process. Adaptive processing schemes require that these sets of measurements, that are provided at the input of an AIC processor, be in phase. Therefore, it is important to assess the phase information of the SOC process with respect to the phase of the conventional CT data acquisition process.

For the sake of simplicity and without any loss of generality, let us assume that we have a CT system that provides sinograms,

$$\{g_{n_{\mathrm{CT}}}(\sigma(n),\beta(t),t_j),(n=1,...,N),(j=1,...,M)\}, \tag{10}$$

that correspond to a stationary tomographic image of interest, where the term t_j represent the time moment $j\Delta t$. Furthermore, let us assume that the organs of the above-mentioned tomographic image follow a generic motion pattern, and that the corresponding sinogram of the tomographic image including organ motion effects is expressed by

$$\{g_{n_{\mathrm{mov}}}(\sigma(n),\beta(t),t_j),(n=1,...,N),(j=1,...,M)\}, \tag{11}$$

which are acquired by the same CT system as the sinogram of Eq. (10). Then, the algebraic difference between the sinograms of Eqs. (10) and (11) should be the output of an optimum CT system that would allow for instantaneous correction of organ motion effects. In particular, let us assume this difference to be denoted by

$$\Delta f_n(\sigma(n),\beta(t),t_j) = g_{n_{\mathrm{mov}}}(\sigma(n),\beta(t),t_j) - g_{n_{\mathrm{CT}}}(\sigma(n),\beta(t),t_j) \quad \text{for } \{(n=1,...,N),(j=1,...,M)\}. \tag{12}$$

If a CT system makes available measurements of the sinograms $\Delta f_n(\sigma(n),\beta(t),t_j)$ and $g_{n_{\mathrm{mov}}}(\sigma(n),\beta(t),t_j)$, then because of Eq. (12), their algebraic difference would provide estimates of $g_{n_{\mathrm{CT}}}(\sigma(n),\beta(t),t_j)$ which is an optimum sinogram without organ motion artifacts. Therefore, there needs to be a direct relationship between the measurements provided by the SOC with those of Eq. (12). Because of Eq. (9), a physical interpretation of the measurements provided by the SOC process can be derived from Eq. (8), which may be rewritten as

$$\frac{\Delta g_{n_o}(\sigma(n_o),\beta(t),t_o+\Delta t)}{\Delta t} = \frac{g_n(\sigma(n),\beta(t_o+\Delta t),t_0+\Delta t)-g_n(\sigma(n),\beta(t_o+\Delta t),t_o)}{\Delta t}. \tag{13}$$

If both terms of Eq. (13) are integrated over a number of m incremental periods during rotation, then the integral is defined by

$$\int_{t=t_0}^{t_0+m\Delta t}\Delta g_n(\sigma(n),\beta(t),t)dt = \sum_{j=1}^{m}\{g_{n_{s1}}^{t_{j+1}}(\sigma(n),\beta(t_{j+1}),t_{j+1}) - g_{n_{s2}}^{t_j}(\sigma(n),\beta(t)_{j+1}),t_j)\}, \tag{14}$$

where, $(n=1,...,N)$, $(m=1,...,M)$. For simplicity, let us express $g_{n_{s1}}^{t_{j+1}}(\sigma(n),\beta(t_{j+1}),t_{j+1})$ and $g_{n_{s2}}^{t_j}(\sigma(n),\beta(t_{j+1}),t_j)$ as g_n^j and g_n^{j+1}, and their difference as Δg_n^{j+1}, where the references to s_1 and s_2 are omitted since they do not impact the measurements. Then the integration process of Eq. (14) is rewritten as

$$\int_{t=t_0}^{t_o+m\Delta t}\Delta g_n(\sigma(n),\beta(t),t_j)dt = (\Delta g_n^1)\rho_1+(\Delta g_n^2)\rho_2+\cdots+(\Delta g_n^m)\rho_m$$

or

$$\int_{t=t_0}^{t_0+m\Delta t}\Delta g_n(\sigma(n),\beta(t),t_j)dt = \int_{j=1}^{m-1}\Delta g_n(\sigma(n),\beta(t),t_j)dt+(\Delta g_n^m)\rho_m, \tag{15}$$

where the scalar factors ρ_m account for angular variation of the detector array during data acquisition, as depicted in Fig. 2.

For the simple case of linear motion effects, the above-mentioned scalar factors take the value, $\rho_m=1$ for $m=1,...,M$. This simple case is analyzed with simulations in Sec. II D. Moreover, when $\rho_m=1$ for $m=1,...,M$, Eq. (15) is reduced to

$$\int_{t=t_0}^{t_o+M\Delta t}\Delta g_n(\sigma(n),\beta(t),t_j)dt = g_n^M-g_n^0. \tag{16}$$

Then, because of Eq. (7),

$$\begin{aligned} g_n(\sigma(n),\beta(t),t_M) &= \int\int f(x,y,t_M)\,\delta\{x\cos[\sigma(n)+\beta(t)]+y\sin[\sigma(n)+\beta(t)]-R\sin\sigma(n)\}dx\,dy, \\ g_n(\sigma(n),\beta(t),t_0) &= \int\int f(x,y,t_0)\,\delta\{x\cos[\sigma(n)+\beta(t)]+y\sin[\sigma(n)+\beta(t)]-R\sin\sigma(n)\}dx\,dy, \end{aligned} \tag{17}$$

which indicate that the two sets of projections, previously mentioned $g_n^M(\sigma(n),\beta(t),t_o+M\Delta t)$ and $g_n^0(\sigma(n),\beta(t_o),t_o)$, have been derived from two different images, $f(x,y,t=t_o+M\Delta t)$ and $f(x,y,t=t_o)$, respectively. How-

ever, the sinogram $g_n^0(\sigma(n),\beta(t),t_0)$ that is derived from the image $f(x,y,t=t_0)$ does not have any kind of motion artifacts because it is defined at $t=t_0$, which is the starting point of the CT data acquisition process, as depicted in Fig. 3. Furthermore, the sinogram $g_n^M(\sigma(n),\beta(t),t_0+M\Delta t)$ is derived from the image $f(x,y,t=t_0+M\Delta t)$, which includes all the motion effects and artifacts recorded during the period $T=M\Delta t$ that is one full cycle of the CT data acquisition process. Thus, the two sinograms, mentioned previously are identical to those defined in Eq. (12), or

$$g_n^0(\sigma(n),\beta(t),t_0)=g_{n_{\mathrm{CT}}}(\sigma(n),\beta(t),t),$$
$$g_n^M(\sigma(n),\beta(t),t_o+M\Delta t)=g_{n_{\mathrm{mov}}}(\sigma(n),\beta(t),t). \tag{18}$$

As a result of Eq. (18) and Eqs. (12) and (14), the integration process of the SOC measurements is identical to the ideal case of the sinogram difference between the stationary sinogram and the conventional sinogram including organ motion defined in Eq. (12) and expressed by

$$\Delta f_n(\sigma(n),\beta(t),t_j)=\int_{t_0}^{t_0+j\Delta t}\Delta g_n(\sigma(n),\beta(t),t)dt. \tag{19}$$

For CT system applications, however, the integration process of the output results of the SOC is not a simple problem. This is because the scalar factors ρ_m, $m=1,...,M$, would induce dc offsets, as shown in the simulations of Sec. II D. The impact of the scalar factors ρ_m on the integration process of Eq. (14) may be removed by means of a normalization process[17] or adaptive processing.[10–12]

It is of interest to note also that if a differentiation process is applied at the right-hand side of Eq. (15), it would remove the cumulative effect of the scalar factors ρ_m. Moreover, because of Eqs. (16) and (19), the derivative of the ideal set of measurements, $\Delta f_n(\sigma(n),\beta(t),t_j)$, which define the difference between the sinograms corresponding to the tomography image with the organ motion effects with those acquired by a CT system without the motion effects, should predict the measurements of the SOC process,

$$\Delta g_n(\sigma(n),\beta(t),t_j)=\frac{d}{dt}[\Delta f_n(\sigma(n),\beta(t),t_j)]. \tag{20}$$

This suggests that Eq. (8) or *the measurements provided by the SOC are the derivative of the difference of the sinograms corresponding to the tomographic image with the organ motion effects and that acquired by a CT system without the motion effects*. In other words, Eq. (13) indicates that the measurements of the SOC process form the basis of a new processing scheme to remove motion artifacts associated with the CT data acquisition process. In particular,

$$\Delta f_n(\sigma(n),\beta(t),t_M)\approx\sum_{j=1}^{M}\Delta g_n(\sigma(n),\beta(t),t_j)$$
$$\text{for}\ \ (n=1,2,...,N) \tag{21}$$

shows that a temporal integration of the output measurements of the SOC provides estimates of the measurements expressed by Eq. (12); or in practical terms we have a new CT system design that generates two types of sinograms; conventional CT sinograms $\{g_{n_{\mathrm{mov}}}(\sigma(n),\beta(t),t_j)$ for $(n=1,...,N)$, $(j=1,...,M)\}$ with motion effects, SOC measurements $\Delta g_n(\sigma(n),\beta(t),t_j)$ that provide by means of integration, as in Eq. (21), estimates of $\Delta f_n(\sigma(n),\beta(t),t_j)$ (for $j=1,...,M$). Then, according to Eq. (12), correction of motion artifacts is derived from a simple algebraic operation:

$$g_{n_{\mathrm{CT}}}(\sigma(n),\beta(t),t_j)=g_{n_{\mathrm{mov}}}(\sigma(n),\beta(t),t_j)$$
$$-\Delta f_n(\sigma(n),\beta(t),t_j). \tag{22}$$

In case of nonlinear effects, which require an estimation or normalization process[17] for the scalar factors ρ_m, alternative optimum estimates of $\Delta f_n(\sigma(n),\beta(t),t_j)$ can be provided by an AIC process with the sinograms $g_n(\sigma(n),\beta(t),t_j)$ and $\Delta g_n(\sigma(n),\beta(t),t_j)$ as inputs, as discussed in Sec. II D.

D. Simulations and system concept demonstration

The simulations were based on the Shepp–Logan phantom as a test image.[18] The software consisted of four signal processing components:

(1) the projection data generation based on a test phantom,
(2) the image reconstruction algorithm, which was the filtered backprojection method including a Ram–Lak filter cascaded with the Parzen window,
(3) the SOC and AIC signal processing concepts described in this paper, and
(4) the image display.

The geometry in the simulations and the rest of the parameters were similar to those of Siemens Somatom Plus 4 x-ray CT medical imaging system. In particular, the simulations included $T=0.75$ s period of rotation for the CT system with a set of $M=1056$ projections by a $N=768$ array of detectors. The choice of this Siemens scanner is because the SOC has been tested with real data sets from the abovementioned real time system provided by a Siemens Somatom Plus 4 system. The lower row of images in Fig. 4 shows various phases of a reconstructed Shepp–Logan phantom that includes simulated motion of the center circle taking place during the data acquisition period of the CT scanner. The rest of the components of the phantom were assumed stationary.

The sinograms at the top part of Fig. 4 present the intermediate output results of the processing steps discussed in Sec. II C. The case of a circular object centered at the origin of the coordinate frame and undergoing radial deformation is described here. This scenario represents a perfectly linear case. In particular, the leftmost sinogram and the second sinogram from the left of Fig. 4 correspond to the tomographic image with the organ motion effects, $g_{n_{\mathrm{mov}}}(\sigma(n),\beta(t),t_j)$ and the output of the SOC, $\Delta g_n(\sigma(n),\beta(t),t_j)$, respectively. The third sinogram from the left represents the temporal integration process, $\Sigma_{j=1}^{M}\Delta g_n(\sigma(n),\beta(t),j\Delta t)$, of the output of the SOC process. This sinogram is identical to that of $\Delta f_n(\sigma(n),\beta(t),t_j)$ that is derived from the ideal case de-

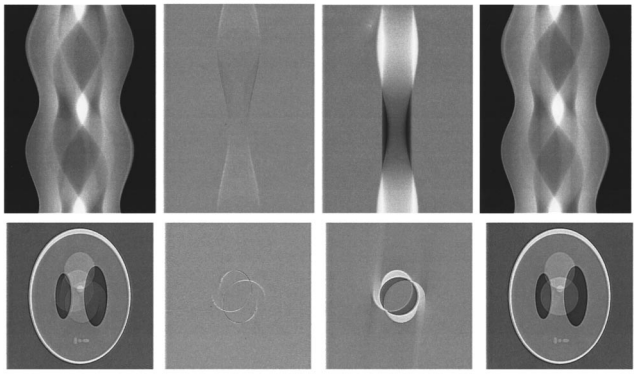

FIG. 4. Processing steps for linearly deforming circle at center of coordinate frame. Top row from left to right: (a) sinogram from conventional CT data acquisition; (b) sinogram from spatial overlap correlator; (c) sinogram derived from linear integration of spatial overlap correlator measurements; (d) correct sinogram computed from conventional CT sinogram and linear integral of SOC measurements. Bottom row from left to right: (e) conventional CT image; (f) image from spatial overlap correlator measurements; (g) image from linear integral of SOC measurements; (h) corrected image.

fined by Eq. (13). Finally the last sinogram is derived from the algebraic difference between the sinograms $g_{n_{\text{mov}}}(\sigma(n),\beta(t),t_j)$ and $\Sigma_{j=1}^{M}\Delta g_n(\sigma(n),\beta(t),j\Delta t)$.

The corresponding reconstructed images are shown directly below each of the sinograms. The leftmost image is blurred because of the motion artifacts. The second image from the left in the lower row of Fig. 4 shows the information tracked by the SOC. As expected, this image shows only the moving components during the data acquisition period. The third image from the left shows the image that corresponds to the linear integral of the SOC measurements, $\Sigma_{j=1}^{M}\Delta g_n(\sigma(n),\beta(t),t_j)$. The last image in the lower row provides a reconstructed image without motion artifacts. This simple example validates Eq. (16), which describes the instantaneous correction of organ motion artifacts for *linear* cases. The same results can be derived by using an AIC process as discussed in Sec. II E. Although the above-mentioned simulations represent a very simple case of organ motion artifacts, their practical significance and aim is to provide a physical interpretation of the processing steps of this investigation, as defined by Eq. (22). If the deformation is nonlinear, as would be the case if instead of a deforming circle centered at the origin, the object is noncircular, or not centered at the origin, the above-given processing steps are not sufficient to correct for motion artifacts.

As an example, Fig. 5 shows the detector time series that result from the above-given processing concept and for a nonlinear case of organ motion. In particular, the solid line of the top diagram of Fig. 5 shows the hypothetical difference of measurements $\Delta f_{n=530}(\sigma(n),\beta(t),t_j)$, $j=1,...,4M$ for the sensor $n=530$. The solid line of the lower diagram of Fig. 5 shows the SOC measurements $\Delta g_{n=530}(\sigma(n),\beta(t),t_j)$, $j=1,...,4M$, as defined by the output of the SOC of Eq. (8). The dashed line of the lower diagram provide the measurements derived as a derivative of the ideal estimates $\Delta f_{n=530}(\sigma(n),\beta(t),t_j)$, $j=1,...,4M$, which are identical to those of the SOC process, $\Delta g_{n=530}(\sigma(n),\beta(t),t_j)$, $j=1,...,4M$, and demonstrate the validity of the results shown by Eq. (20). Although these results appear to be promising, temporal integration of the estimates of the SOC process $\Delta g_{n=530}(\sigma(n),\beta(t),t_j)$, $j=1,...,4M$, according to Eq. (21), which are shown by the dashed line at the top diagram of Fig. 5, do not predict the estimates of $\Delta f_{n=530}(\sigma(n),\beta(t),t_j)$, $j=1,...,4M$. Furthermore, the same results indicate that the temporal integration of the SOC output estimates induces dc offsets, which are generated by the fact that the scalar factors ρ_m defined in Eq. (15) have not been considered in the linear integration process. Moreover, the dc offsets in these results suggest that the model in Eq. (15) is correct. Since the results of Fig. 5 refer to the information recorded by the detector $n=530$ of the $N=768$ receiving array, it is essential to note that as this detector ($n=530$) rotates around the tomography area of interest, it does not have a continuous view of the moving object. For detectors having a continuous view of the moving object the corresponding results are different from those of Fig. 5. Figure 6 presents the same information as Fig. 5, but for the detector $n=384$.

It is apparent from these results that integration of the measurements $\Delta g_{n=384}(\sigma(n),\beta(t),t_j)$, $j=1,...,4M$, of the SOC process follow the model of radial deformation with values for the scalar factors, $\rho_m=1$, $n=1,...,M$ and according to Eq. (21) provide estimates of $\Delta f_{n=384}(\sigma(n),\beta(t),t_j)$, $j=1,...,4M$. The sinograms of Fig. 7 provide the same information as that of Figs. 5 and 6 but for all the received signals of the CT receiving array. In particular, the top left sinogram shows the measurements of the SOC, $\Delta g_n(\sigma(n),\beta(t),_j t_j)$ for $(j=1,...,M)$ $(n=1,...,N)$, for one complete cycle of the CT acquisition process. The top right sinogram presents the results of the linear integration process $\Sigma_{j=1}^{M}\Delta g_n(\sigma(n),\beta(t),t_j)$ for $(j=1,...,M)$ $(n=1,...,N)$. The bottom sinogram shows the expected estimates of $\Delta f_n(\sigma(n),\beta(t),t_j)$ for $(j=1,...,M)$ $(n=1,...,N)$, which are supposed to be identical to the output of the integration of the SOC measurements. It is apparent from the results of Fig. 7 that the effects of the dc offset of Eq. (15) have destroyed the information provided by the SOC process. These dc effects were caused by the fact that the values of the scalar factors were assumed to be $\rho_m=1$, $n=1,...,M$, as is also shown by the results of Fig. 5.

As discussed before, methods to remove these dc effects from the temporal integration estimates of the SOC output results could include the use of normalizers,[17] or optimally by the AIC,[10–12] which is discussed next.

E. Adaptive processing for removing CT motion artifacts

The relationship in Eq. (15) forms the basis for the implementation of an AIC method[10–12] to remove the organ motion artifacts. However, the attempt in this section to provide estimates for the scalar factors ρ_m should be considered to be a preliminary effort, since the reported results have been tested with simulations that represent a perfect case scenario.

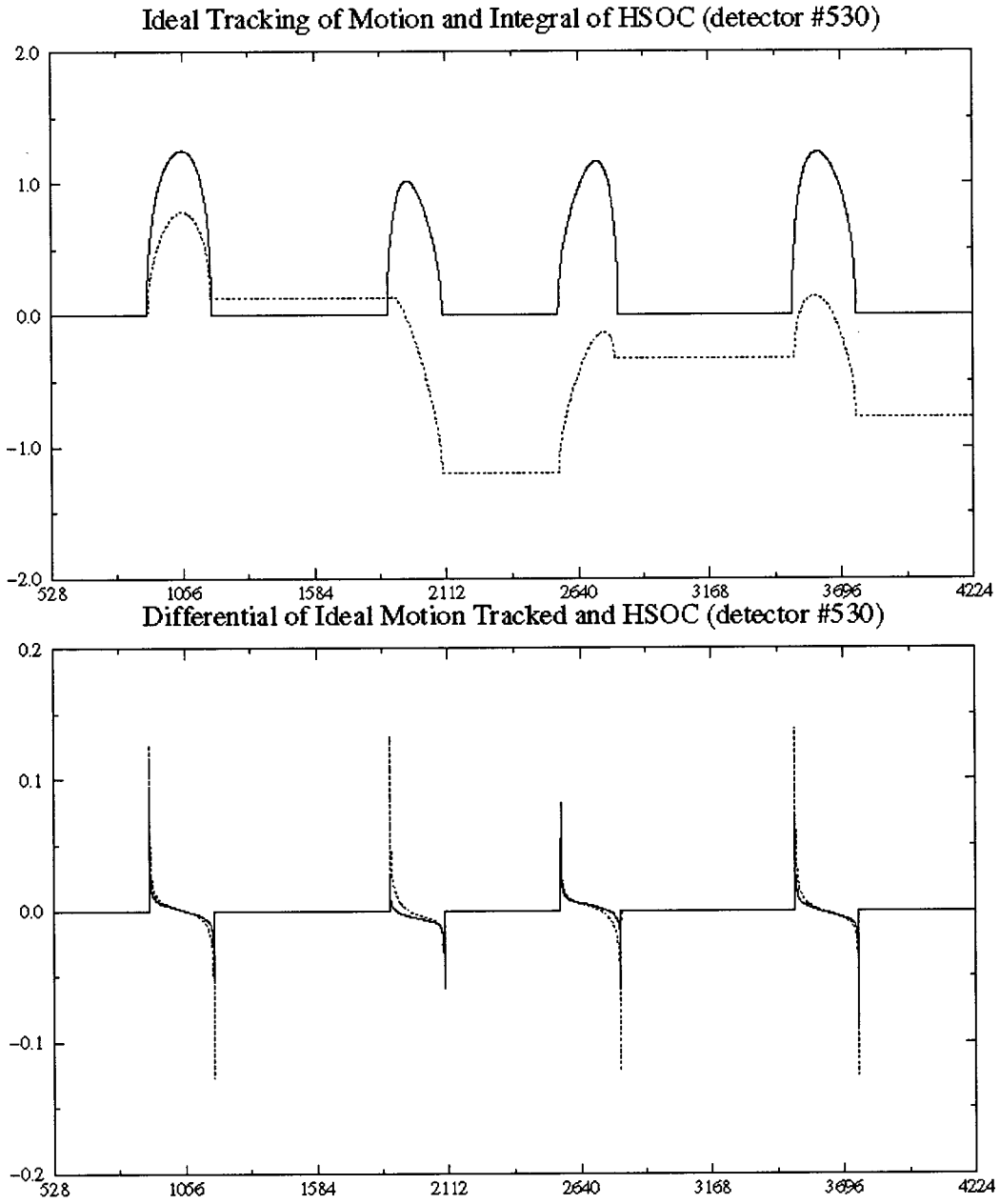

FIG. 5. Interpretation of the physical process associated with the measurements of the spatial overlap correlator for the sensor $n=530$ and their comparison with the predicted estimates according to the model expressed by Eqs. (13), (14), (16), and (20).

Any attempt to implement the adaptive concept of this investigation in real time CT systems should consider many other parameters such as the system errors associated with the implementation process of the SOC in a specific real time CT system of interest. The processing structure of an AIC[10–12] is shown in Fig. 8. This technique is useful when any noise interference that is present in a signal is measured accurately. The algorithms used in this investigation are the LMS and NLMS algorithms.[11,12] They were chosen because the model in Eqs. (15) and (16) represents a linear combination of the weights ρ_m and the SOC outputs, $\Delta g_n(\sigma(n),\beta(t),t_j)$.

Let us start with a very brief description of the AIC concept, as defined in Fig. 8. The received noisy signal by a detector is defined by $y(j\Delta t)=s(j\Delta t)+n(j\Delta t)$, where $s(j\Delta t)$ and $n(j\Delta t)$ are the signal and noise components, respectively. In an AIC system with performance feedback it is essential that either the signal, $y(j\Delta t)$, and the noise, $n(j\Delta t)$, components are either available or measured simultaneously. Assume that an adaptation process with performance feedback provides the weight vector to the linear combiner to generate estimates of the noise $n(j\Delta t)$. In general the adaptation process includes minimization of the mean-square value of the error signal defined by the performance feedback. Optimization by this criterion is common in many adaptive and nonadaptive applications. Widrow[10] points out that in adaptive systems considerable ingenuity is often required to find a suitable signal (or noise) to define this optimization process, since if the actual desired response

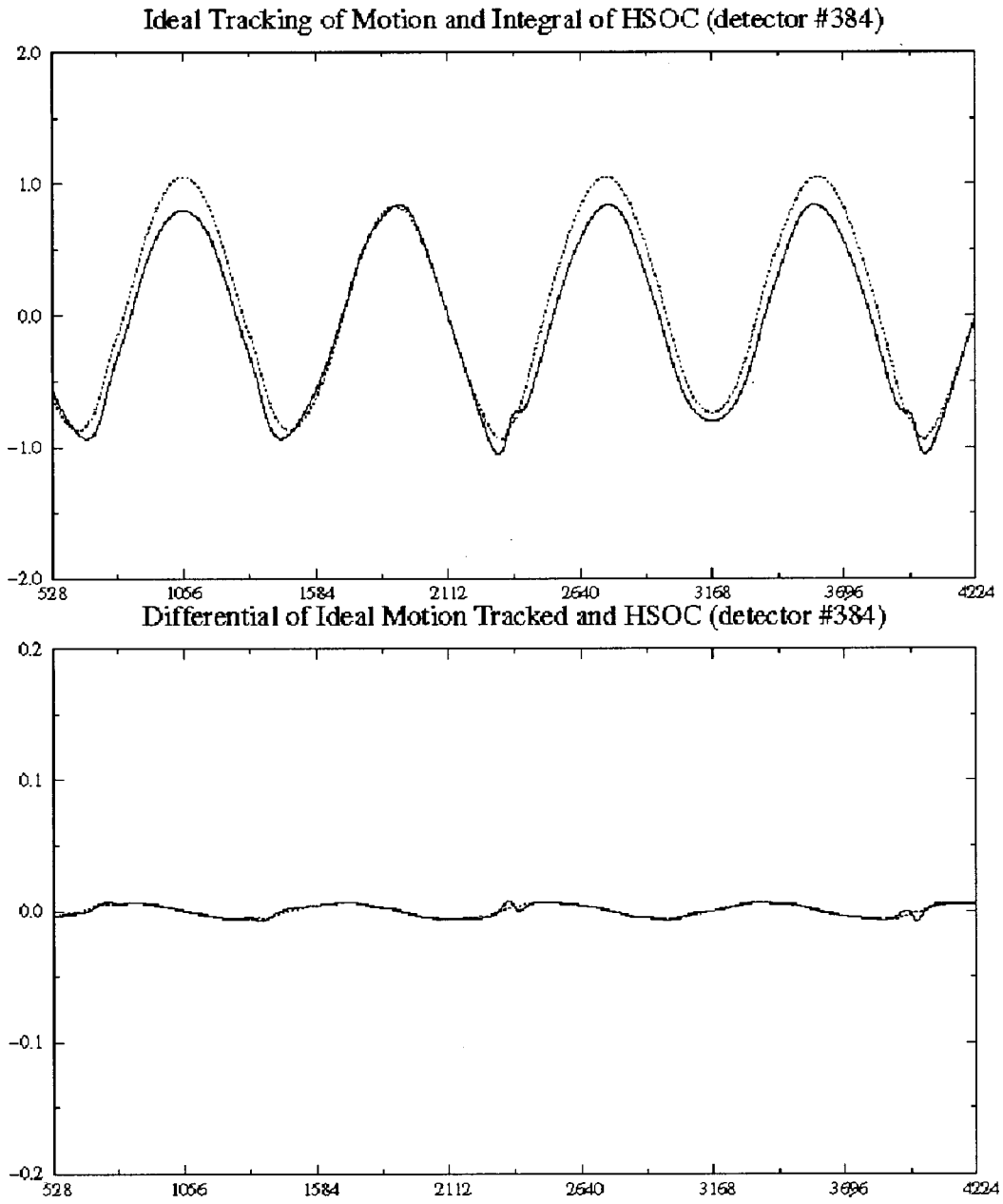

FIG. 6. Interpretation of the physical process associated with the measurements of the spatial overlap correlator for the sensor $n=384$ and their comparison with the predicted estimates according to the model expressed by Eqs. (13), (14), (16), and (20).

of the system were available one would generally not need the adaptive system. In our case, the measurements provided by the SOC $\Delta g_n(\sigma(n),\beta(t),t_j)$ form the basis of the noise estimates for the adaptation process, as will be analyzed in this section.

Assume that the noise measurements at the input of the adaptation process in Fig. 8 are provided by the input vector $\overline{X}$ with terms $[x(\Delta t),x(2\Delta t),\ldots,x(M\Delta t)]^T$. Furthermore, the output of a least mean square adaptation process (LMS),[11] $u(j\Delta t)$ is a linear combination of the input measurements $\overline{X}$ and the weight adaptive coefficients $[w(\Delta t),w(2\Delta t),\ldots,w(M\Delta t)]^T$ of the vector $\overline{W}$. Then, the output of an AIC is given by

$$\overline{\varepsilon}=\overline{Y}-\overline{X}^T\overline{W}, \tag{23}$$

where $\overline{Y}$ is the input vector of the noise measurements, $y(j\Delta t)$ for $j=1,2,\ldots,M$, and M is the maximum number of samples to be processed. Widrow's AIC concept[10] is based on the minimization of the square of Eq. (23), $E_{\min}[(\overline{\varepsilon})^2]=E_{\min}[(\overline{S}+\overline{N})^2]-E_{\min}[(\overline{X}^T\overline{W})^2]$, which suggests that when $E[\overline{\varepsilon}]$ is minimized with signal power $E[\overline{S}]$ is unaffected, then the term $E[(\overline{N}-\overline{X}^T\overline{W})^2]$ is minimized. Optimum values of $\overline{W}$ that minimize $\overline{\varepsilon}$ are derived by descending toward the minimum of the performance feedback surface. This suggests that the output of the AIC process $E_{\min}[\overline{\varepsilon}]=E[\overline{S}]$ pro-

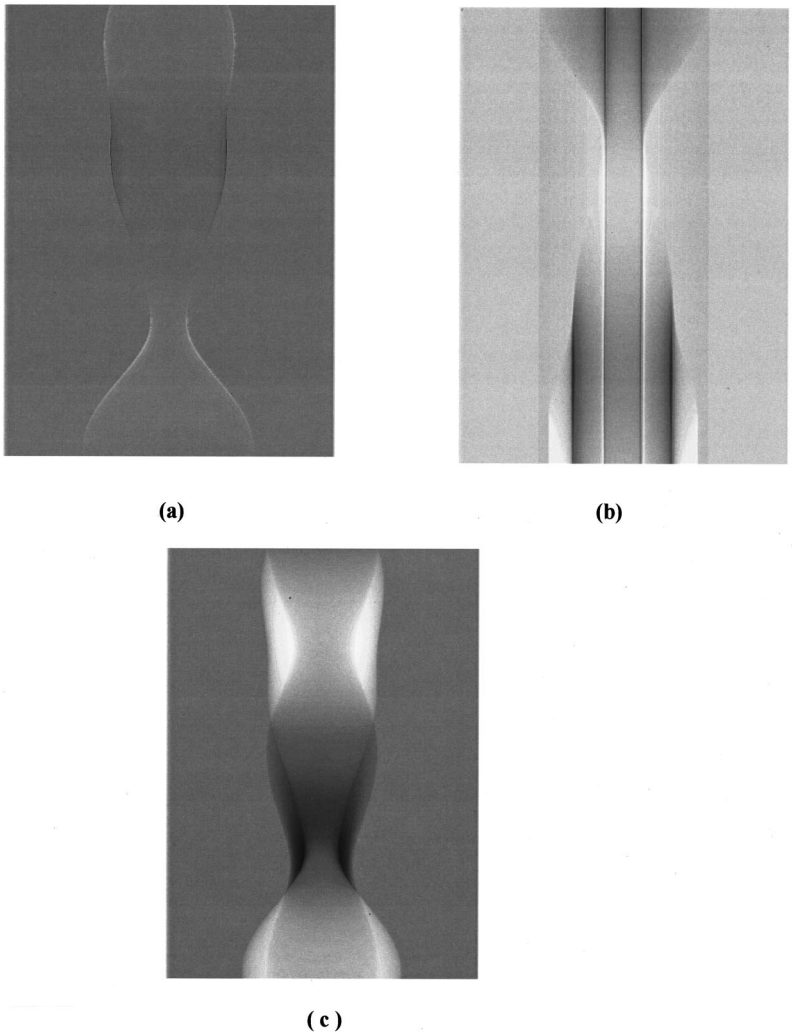

FIG. 7. Interpretation of the physical process associated with the sinogram measurements of the spatial overlap correlator for all the sensors and their comparison with the predicted estimates according to the model expressed by Eqs. (13), (14), (16), and (22): (a) sinogram output of SOC, (b) sinogram that results from temporal integration of sinogram (a) according to Eq. (22), and (c) prediction for sinogram (b) according to Eq. (13).

vides estimates of the signal vector. The output $u(j\Delta t)$ of an adaptive filter (LMS or NLMS algorithms)[11,12] with L adaptive weights $(w_1, w_2, \ldots, w_L)$ and for an interference input $x(j\Delta t)$ at time $j\Delta t$ are given by

$$u(j\Delta t) = \sum_{i=1}^{L} w_i^{j\Delta t} \times x((j+i-L)\Delta t). \tag{24}$$

For the LMS and NLMS algorithms,[11,12] the update equations for the adaptive weights are given in Eqs. (25) and (26), respectively,

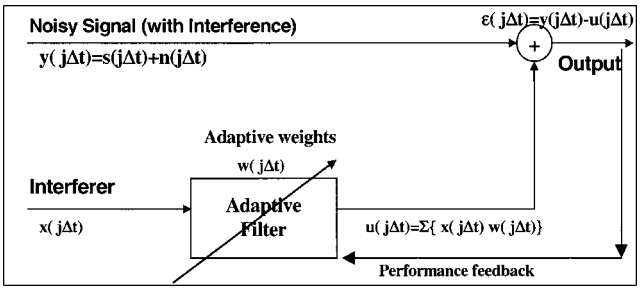

FIG. 8. Concept of adaptive interference canceller (Ref. 10, p. 303).

$$w_i^{(j+1)\Delta t} = w_i^{j\Delta t} + (\mu \times x((j+i-L)\Delta t) \times u(j\Delta t)), \quad (i = 1,2,\ldots,L), \tag{25}$$

where μ is the adaptive LMS step size parameter,

$$w_i^{(j+1)\Delta t} = w_i^{j\Delta t} + \left(\frac{\lambda}{\alpha + |n|} \times x((j+i-L)\Delta t) \times u(j\Delta t) \right), \quad (i = 1,2,\ldots,L). \tag{26}$$

Here λ is the NLMS step size parameter, α is a stability parameter, and $|n|$ is the Euclidean norm of the vector $[x((j+1-L)\Delta t), x((j+2-L)\Delta t), \ldots, x(j\Delta t)]$.

To demonstrate the effiency of the AIC processor at removing interferences, a synthetic noisy signal $y(j\Delta t)$, and an interferer $x(j\Delta t)$ that is assumed to be accurately measured were considered. The output of the AIC process, $u(j\Delta t)$, is defined by Eqs. (23), (24), and (26).

Real results from the output of the AIC process defined by Eqs. (24), (25), and (26) to remove noise component from received noisy signal are shown in Fig. 9. The upper graph of Fig. 9 shows the noisy signal, $y(j\Delta t)$, that includes the acoustic signal of heart beats recorded with an electronic stethoscope near the noisy intense environment of an operat-

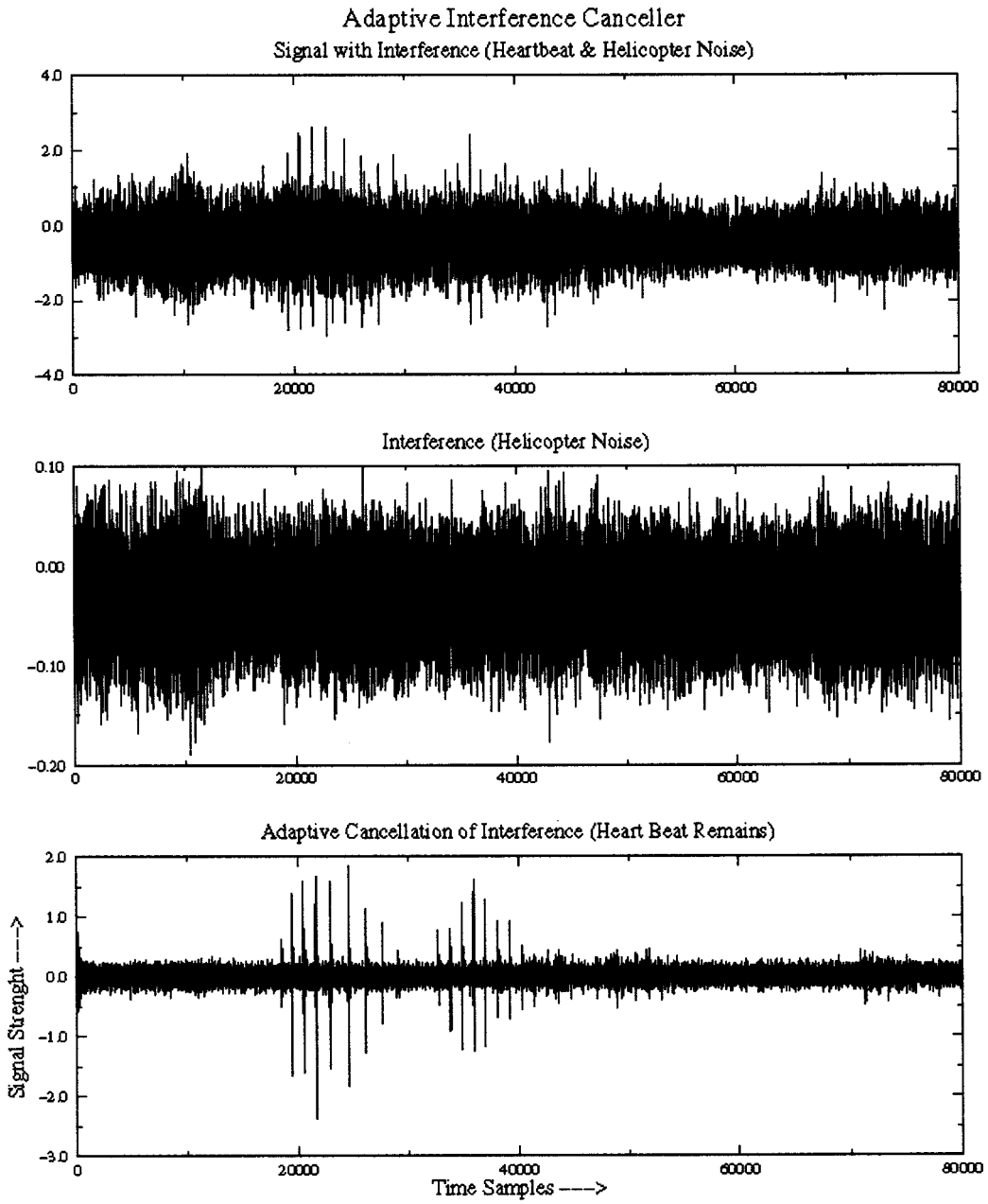

FIG. 9. Real results from output of adaptive interference canceller to remove noise component from received noisy signal. Upper graph: The noisy signal that includes the acoustic signal of heart beats with electronic stethoscope near the noise intense environment of an operating helicopter. Middle graph: The noise of the helicopter recorded by another stethoscope simultaneously with the noisy signal shown by the upper graph. Bottom graph: The output of the AIC process that has suppressed successfully by 8 dB the helicopter noise leaving the acoustic signal of interest (heart beats) as the principal information in the recorded signal.

ing helicopter. The middle graph shows the interference $x(j\Delta t)$, which is the noise of the helicopter recorded by another stethoscope, simultaneously with the noisy signal. The bottom graph shows the output of the AIC process $\varepsilon(j\Delta t)$ that has suppressed successfully by 8 dB the helicopter noise leaving the acoustic signal of interest (heart beats) as the principal information in the recorded signal. It is evident from Fig. 9 that the AIC is successful at completely removing the interference $x(j\Delta t)$ and leaves the signal of interest undistorted.

The above-mentioned implementation concept of the AIC process makes it an ideal tool for removing any motion artifacts present in the reconstructed images of CT systems that include the SOC concept as defined previously. Organ motion $\Delta g_n(\sigma(n),\beta(t),t_j)$ tracked at the sensor level by the SOC can be treated as the interference measurements $x(j\Delta t)$, and are introduced as input to the AIC. The original sensor time series (sinograms) $g_{n_{\text{mov}}}(\sigma(n),\beta(t),t_j)$ of a conventional CT system are treated as the "noisy" input signal $y(j\Delta t)$ of the AIC process (23), which will have as output $\varepsilon(j\Delta t)$, the corrected sinograms $\overline{g}^{*}_{\text{CT}}$

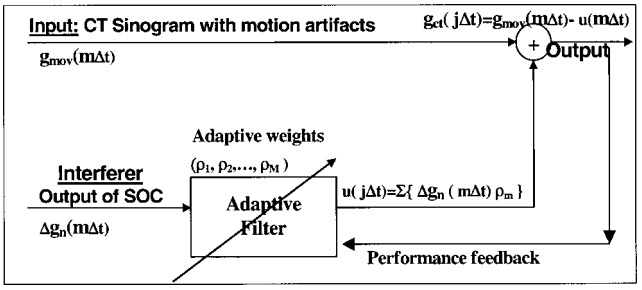

FIG. 10. Concept of adaptive interference canceller and spatial overlap correlator for removing motion artifacts in CT medical imaging applications.

$=\lfloor g_{n_{CT}}((t_1), g_{n_{CT}}((t_2), \ldots g_{n_{CT}}((t_M)\rfloor$, for $n=1,2,\ldots,N$. Thus, the AIC processing flow in Fig. 8 is modified accordingly to meet the new requirements. Let us start with the basic equation that defines the adaptive process for the CT problem of this investigation,

$$\overline{g}_{CT}=\overline{g}_{mov}-P_n\overline{\Delta g}, \tag{27}$$

where, the vectors $\overline{g}^*_{CT}=[g_{n_{CT}}((t_1), g_{n_{CT}}((t_2), \ldots, g_{n_{CT}}((t_M)]$ and $\overline{g}^*_{mov}=\lfloor g_{n_{mov}}((t_1), g_{n_{mov}}((t_2), \ldots, g_{n_{mov}}((t_M)\rfloor$ are defined by Eqs. (10) and (11), respectively, one for each of the detectors $n=1,2,\ldots,N$, of the receiving CT array, $\overline{\Delta g_n}^*=[\Delta g_n((t_1), \Delta g_n((t_2), \ldots, \Delta g_n((t_M)]$ is the vector of the SOC output, which represents the noise measurements and the matrix P_n includes the adaptive weights for each sensor n, defined by

$$P_n=\begin{bmatrix} \rho_1 & 0 & 0 & 0 \\ \rho_1 & \rho_2 & 0 & 0 \\ . & . & . & . \\ \rho_1 & \rho_2 & . & \rho_M \end{bmatrix}. \tag{28}$$

Equation (27) represents the CT temporal measurements, $m=1,2,\ldots,M$ of one complete CT rotation. For a set of two continuous rotations and for the CT temporal measurements $m=M+1,M+2,\ldots,2M$ Eq. (27) is simplified as follows:

$$\overline{g}_{CT}=\overline{g}_{mov}-\overline{\Delta g}^T\overline{W}, \tag{29}$$

where the vectors $\overline{g}_{CT}=[g_{n_{CT}}((t_{M+1}), g_{n_{CT}}((t_{M+1}), \ldots, g_{n_{CT}}((t_{2M})]^T$ and $\overline{g}_{mov}=[g_{n_{mov}}((t_{M+1}), g_{n_{mov}}((t_{M+1}), g_{n_{mov}}((t_{M+2}), \ldots, g_{n_{mov}}((t_{2M})]^T$ are defined by Eqs. (10) and (11), respectively, for each one of the detectors $n=1,2,\ldots,N$, of the receiving CT array, $\overline{\Delta g_n}=[\Delta g_n((t_{M+1}), \Delta g_n((t_{M+2}), \ldots, \Delta g_n((t_{2M})]^T$ is the vector of the SOC output, which represents the noise measurements and the vector $\overline{W}=[\rho_1, \rho_2, \ldots, \rho_M]^T$ are the linear adaptive weights. The adaptive weights are computed according to the model of Eq. (23) and defined by Eqs. (25) and (26) for the LMS and NLMS algorithms, respectively, with initial condition $\rho_m=1$, $n=1,\ldots,M$. Figure 10 shows the adaptive processing flow for a medical CT system that includes the implementation of the SOC in the data acquisition functionality of this system. Thus, LMS or NLMS adaptive algorithms form the basis of an iterative estimation process for the terms $(g_n^{m-1}-g_n^{m-2})\rho_{m-1}$ and a summation step, as defined in Eq. (15) that defines the temporal integration of the SOC output, which is a predictive estimate for the term, $\Delta f_n(\sigma(n), \beta(t), t_j)$, of Eq. (12). The output of this AIC process provides predictive estimates for sinograms that have been corrected for motion artifacts according to the information provided by the measurements of the SOC. Therefore, if the output sinogram $\overline{g}_{CT}=[g_{n_{CT}}((t_{M+1}), g_{n_{CT}}((t_{M+1}), \ldots, g_{n_{CT}}((t_{2M})]^T$ of the AIC process is provided at the input of a CT image reconstruction algorithm, then the new image will not include motion artifacts.

Although the consideration of other adaptive methods, such as the RLS algorithms,[13] may be considered in the AIC process shown in Fig. 10, the emphasis of this investigation is to define the concept of an AIC processing structure for motion correction in medical CT applications. When this generic AIC structure is defined, then a variety of adaptive algorithms may be evaluated to address the noise characteristics associated with a specific CT system of interest. Thus, the choice of an adaptive algorithm for the AIC process of Fig. 10 is an implementation issue and is beyond the scope of this investigation. This is because the implementation of the SOC in an operational medical CT system, which is discussed in Sec. III, includes a high cost and it has not been carried out under this study. In what follows, the AIC process is assessed with simulations based on the parameters defined in Sec. II C.

Figure 11 shows simulation results of the concept of the AIC process for CT applications for a more general case, where there is an arbitrarily placed continuously deforming object. The signals in the upper part of Fig. 11 represent the expected measurements $\overline{g}_{CT}=[g_{n_{CT}}((t_{M+1}), g_{n_{CT}}((t_{M+1}), \ldots, g_{n_{CT}}((t_{2M})]^T$ for a test phantom without motion artifacts with the dotted line, and the corresponding sinogram $\overline{g}_{mov}=[g_{n_{mov}}((t_{M+1}), g_{n_{mov}}((t_{M+2}), \ldots, g_{n_{mov}} \times((t_{2M})]^T$ with motion artifacts with the solid line. The signals in the lower part of Fig. 11 show the expected measurements $\overline{g}_{CT}=[g_{n_{CT}}((t_{M+1}), g_{n_{CT}}((t_{M+1}), \ldots, g_{n_{CT}}((t_{2M})]^T$ for a test phantom with the motion artifacts corrected with the dotted line, and the output $\varepsilon(j\Delta t)$, for $j=M+1$, $M+2,\ldots,2M$, of the AIC process when convergence is reached with the solid line. Figure 12 shows the corresponding reconstructed images from this case. The leftmost pair shows the conventional x-ray CT sinogram and image, corresponding to $g_{n_{mov}}(\sigma(n), \beta(t), t_j)$. The SOC measurements and the estimate of the nonlinear integral by the AIC process is shown in the second and third pairs of images from the left. These sinogram and image pairs correspond $\Delta g_n(\sigma(n), \beta(t), t_j)$ and $\Delta f_n(\sigma(n), \beta(t), t_j)$, respectively. Based on the estimate of $\Delta f_n(\sigma(n), \beta(t), t_j)$ and the measured $g_{n_{mov}}(\sigma(n), \beta(t), t_j)$ the optimum sinogram $g_{n_{CT}}(\sigma(n), \beta(t), t_j)$ is computed. This optimum sinogram is shown in the upper right of Fig. 12. The corresponding image in which all motion artifacts have been corrected is shown in the lower right image.

At this point it is important to note that in the results of Figs. 11 and 12, the noise of the simulated CT received sig-

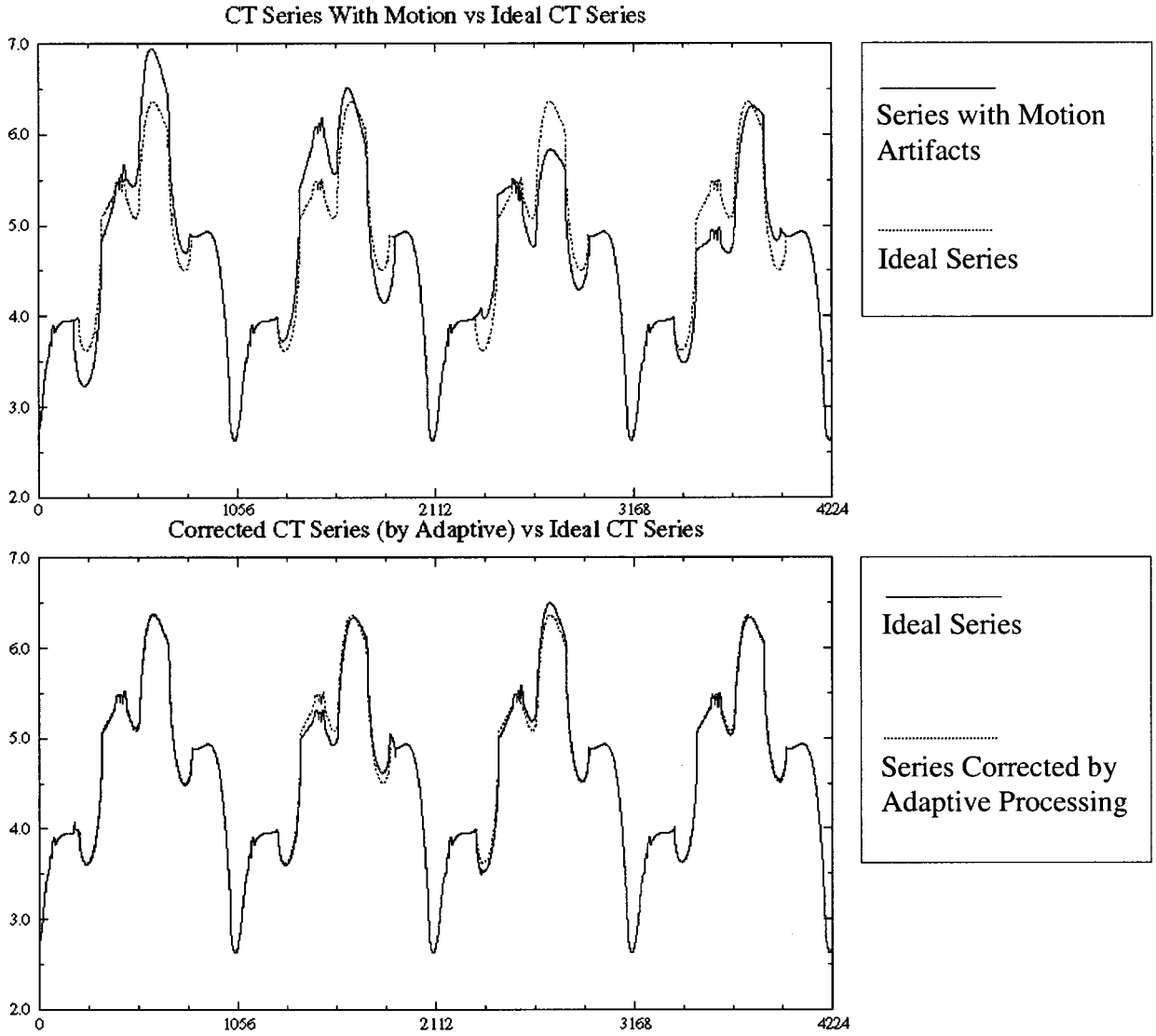

FIG. 11. Simulation results of adaptive interference canceller and spatial overlap correlator concepts for removing motion artifacts in CT medical imaging applications. Upper graph: Signals from sinograms with motion artifacts and without motion artifacts. Lower graph: Comparison of the output of the AIC process with the expected sinogram output without motion artifacts.

nals was considered to be the motion of the left ellipse of the Shepp–Logan phantom. White noise effects have not been considered in this case. This is because the signal-to-noise ratio in CT scanners is very high.

III. SYSTEM IMPLEMENTATION

An essential technical requirement by the SOC is the implementation of two CT x-ray sources separated with an angular spacing equal to the sensor spacing of the receiving array, as shown in Fig. 2. However, because of the massive size of an x-ray source, a physical two-source implementation for a CT scanner is technically not feasible. At this point it is important to acknowledge the valuable contributions in this implementation effort by Siemens Medical AG (Germany). In particular, the family of Siemens CT scanners Somatom-4 include the flying focal point functionality that is used to double the spatial sampling frequency. In this investigation, it is suggested that the second source can be generated by the deviation of the x-ray beam by a magnetic or electric field, which forms the flying focal spot functionality of Siemens Somatom Plus 4, Elscint's Twin RTS, and GE scanners with focal spot wobble. The new active transmission of the flying focal spot functionality defines a new source at an angle $\delta\theta$ and time instant $\Delta t/2$ with respect to the previous source position. Typical values for $\Delta t/2$ are approximately 0.5 ms. This process provides a second set of spatial samples that are offset by $\frac{1}{2}$ sensor spacing in the receiving array, hence it is equivalent to doubling the spatial resolution of a CT fan-beam scanner.

Thus, an implementation effort of the SOC concept in CT systems is to consider the flying focal point functionality to be modified in such a way that will simulate the second source being activated about 0.5 ms later than the previous x-ray transmission. However, the source should be deviated in such a way that the second active transmission should be formed exactly at the same location as the previous one and

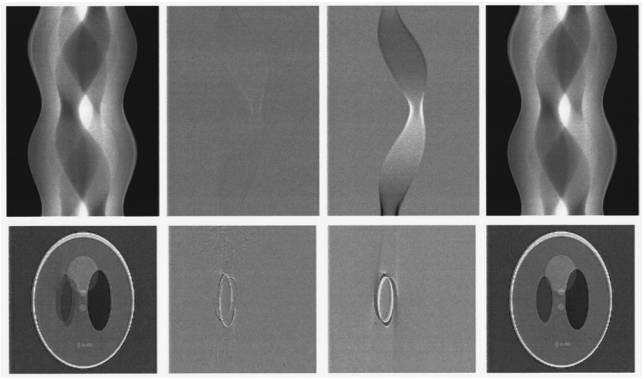

FIG. 12. Processing steps for arbitrarily placed deforming object. Top row from left to right: (a) sinogram from conventional CT data acquisition; (b) sinogram from spatial overlap correlator; (c) sinogram derived from nonlinear integration of spatial overlap correlator measurements by the adaptive interference canceller; (d) correct sinogram computed from conventional CT sinogram and SOC measurements by AIC processing. Bottom row from left to right: (e) conventional CT image; (f) image from spatial overlap correlator measurements; (g) image from nonlinear integral of SOC measurements; (h) corrected image from AIC processing.

with an appropriate realignment of the detector array. It has been assessed that this kind of implementation effort requires costly hardware modifications in existing CT scanners that include the flying focal spot functionality. A critical requirement is the need for perfect source and detector alignment over the two spatially overlapping transmissions. During the course of this investigation, data from a CT system including the hardware implementation of the SOC have not been available to assess the effectiveness of the AIC process. Therefore other alternatives had to be investigated to address this kind of implementation issues. A generic implementation of the SOC has been proposed[14] to track the net amplitude and phase of the organ motion during the data acquisition process. This tracking of the amplitude and phase information has been exploited with alternative motion correction algorithms called the retrospective-SOC gating and coherent sinogram synthesis (CSS) and methods that are based on a software implementation concept of the SOC in x-ray CT scanners.[14,15]

IV. CONCLUSION

The paper discusses a novel approach to tracking and removing organ motion artifacts in CT systems. The method first uses the SOC process to sample information associated with the organ motion present during the conventional CT data acquisition process. An optimum approach to remove the organ motion effects is to apply AIC methods, which treat the output of the SOC process as noise interference at the input of the adaptive processor. Tests with synthetic data sets demonstrate the validity of this generic signal processing methodology, and also prove that it is practically realizable.

In summary, the results of this investigation represent an optimum solution to the overall CT motion correction problem. However, because of practical implementation issues, a nonoptimum system implementation concept for the SOC process has been investigated and is presented in Refs. 14 and 16. This nonoptimum concept has been implemented in x-ray CT medical imaging scanners and has been tested with real data sets using moving phantoms and real patients. The experimental part of the present investigation is focused on cardiac applications for imaging coronary calcification and the results are discussed in the accompanying paper.[14]

ACKNOWLEDGMENTS

The authors wish to express their appreciation to Dr. Klaus Klingenbeck-Regn of Siemens Medical AG, (Forchheim, Germany) and the technical experts of Siemens for the technical discussions and exchanges on the subject matter.

[a]Electronic mail: adhanant@dciem.dnd.ca
[b]Senior Member IEEE; electronic mail: stergios@dciem.dnd.ca
[c]Electronic mail: ilias.iakovides@cec.eu.int

[1] J. D. Godwin, R. S. Breiman, and J. M. Speckman, "Problems and pitfalls in the evaluation of thoracic dissection by computed tomography," J. Comput. Assist. Tomogr. **6**, 750–756 (1982).
[2] R. J. Alfidi, W. J. MacIntyre, and J. R. Haaga, "The effects of biological motion in CT resolution," Am. J. Radiol. **127**, 11–15 (1976).
[3] C. R. Crawford, K. F. King, C. J. Ritchie, and J. D. Godwin, "Respiratory compensation in projection imaging using a magnification and displacement model," IEEE Trans. Med. Imaging **15**, 327–332 (1996).
[4] C. J. Ritchie, J. Hsieh, M. F. Gard, J. D. Godwin, Y. Kim, and C. R. Crawford, "Predictive respiratory gating: A new method to reduce motion artifacts in CT scans," Radiology **190**, 847–852 (1994).
[5] Y. H. Chiu and S. F. Yau, "Tomographic reconstruction Of time-varying object From linear time-sequential sampled projections," Proc. IEEE Conf. ASSP, Adelaide **1**, V309–V312 (1994).
[6] M. Hedley, H. Yan, and D. Rosenfeld, "Motion artifacts correction in MRI using generalized projections," IEEE Trans. Med. Imaging **10**, 40–46 (1991).
[7] C. J. Ritchie, C. R. Crawford, J. D. Godwin, K. F. King, and Y. Kim, "Correction of computed tomography motion artifacts using pixel-specific back-projection," IEEE Trans. Med. Imaging **15**, 333–342 (1996).
[8] S. Stergiopoulos, "Optimum bearing resolution for a moving towed array and extension of its physical aperture," J. Acoust. Soc. Am. **87**, 2128–2140 (1990).
[9] S. Stergiopoulos, "Implementation of adaptive and synthetic aperture processing in real-time Sonar systems," Proc. IEEE **86**, 358–396 (1998).
[10] B. Widrow and S. D. Stearns, *Adaptive Signal Processing* (Prentice–Hall, Englewood Cliffs, NJ, 1985).
[11] L. J. Griffiths and C. W. Jim, "An alternative approach to linearly constrained adaptive beamforming," IEEE Trans. Antennas Propag. **AP-30**, 27–34 (1982).
[12] D. T. M. Slock, "On the convergence behavior of the LMS and the normalized LMS algorithms," IEEE Trans. Acoust., Speech, Signal Process. **31**, 2811–1825 (1993).
[13] A. H. Sayed and T. Kailath, "A state-space approach to adaptive RLS filtering," IEEE Signal Process. Mag. **11**, 18–60 (1994).
[14] A. C. Dhanantwari *et al.*, "Correcting organ motion artifacts in x-ray CT systems based on tracking of motion phase by the spatial overlap correlator. II. Experimental study," Med. Phys. **28**, 1577–1596 (2001).
[15] A. Dhanantwari and S. Stergiopoulos, "A new method tracking motion effects in computed tomography imaging applications," ICSPAT'98 Conf. Proc. **1**, 16–21 (1998).
[16] A. Dhanantwari, "A new method tracking motion effects in computed tomography imaging applications," Ph.D. thesis, Dept. of Elec. & Comp. Eng., The University of Western Ontario, London, Ontario, 1999.
[17] S. Stergiopoulos, "Noise normalization technique for broadband towed array data," J. Acoust. Soc. Am. **97**, 2334–2345 (1995).
[18] A. C. Kak, *Digital Image Processing Techniques* (Academic, New York, 1984).